Desalination and Water Treatment
www.deswater.com

doi: 10.1080/19443994.2013.807033

52 (2014) 1683–1692
February

Taylor & Francis
Taylor & Francis Group

Simulation of a solar thermal membrane distillation: comparison between linear and helical fibers

Adel Zrelli*, Béchir Chaouachi, Slimane Gabsi

Environmental, Catalysis and Process Analysis Research Unity, National Engineering School of Gabes, University of Gabes, Omar Ibn, ElKhattab St., 6029 Gabes, Tunisia
Tel. +75 39 21 00; Fax: +75 39 21 90; email: adel.zrelli@yahoo.fr

Received 16 December 2011; Accepted 28 November 2011

ABSTRACT

In arid coastal regions, the lack of potable water coincides often with high solar insolation. In this case, coupling of the desalination systems with solar energy is of great importance. Among the desalination systems, the membrane distillation technique holds numerous advantages. The present work focuses on the vacuum membrane distillation coupled with solar energy. The aim is to simulate a novel membrane configuration in order to enhance the permeate product. This novel membrane is composed of hollow fiber wound in helically coiled shape. Two-dimensional Navier–Stokes equations are written and then solved using the finite element method. For a pitch of 32.2 mm and a coil radius of 95.7 mm, the simulation results of the permeate product are 0.2685 kg/h and 7.688 10^{-3} kg/sm² for the permeate flux. These values present an enhancement when compared to the linear hollow fiber configuration at the same operating conditions. This enhancement is about 28% for the permeate flow rate.

Keywords: Vacuum membrane desalination; Solar energy; Helical fiber; Linear fiber; Simulation

1. Introduction

Membrane distillation (MD), is a thermal process based on highly porous and hydrophobic membrane. It can be classified into four different configurations according to the nature of the cold side of the membrane [1]. The first configuration is the direct contact membrane distillation in which the membrane is in direct contact with liquid phases in both sides. The volatile components of the feed evaporate at the interface feed/membrane diffuse through the air filling up the membrane pores and condensate at the cold side in the distillate stream [2,3]. The second configuration is air gap membrane distillation in which an air gap is interposed between the membrane and the condensate surface. In this case, the air gap functions as thermal insulation between membrane and condenser wall [4,5]. The sweeping

*Corresponding author.

Presented at the Third Maghreb Conference on Desalination and Water Treatment (CMTDE 2011) Hammamet, Tunisia, 18–22 December 2011

1944-3994/1944-3986 © 2013 Balaban Desalination Publications. All rights reserved.

gas membrane distillation, represents the third configuration. In this configuration, a sweeping gas is used as carrier for the produced vapor. The condensation of this vapor is occurred out of the membrane [6]. The fourth and the last configuration is the vacuum membrane distillation (VMD), in which the vapor phase is vacuumed from the liquid through the membrane and condensed outside of the module [7,8]. This configuration presents many advantages when compared to the conventional separation techniques [9]. The two main advantages are a very low conductive heat loss and a reduced mass transfer resistance [10].

VMD has attracted increasing interest for various applications. From energy consumption point of view, it could clearly compete with reverse osmosis, when coupled with alternate source of energy like solar energy [11]. Different configurations can be used in order to couple VMD and solar energy. Also, membrane can be placed in or out of the absorber of the solar collector. Furthermore, many configurations of the hollow fiber membrane can be used. Among these configurations, we found the linear and the helical fibers.

Few studies have been undertaken on the use of the helical fibers. Mallubhotla et al. [12] have compared, for nanofiltration, the obtained membrane permeation rates in the linear to the helical modules. The results show an enhancement of this rate during their use of the helical module. This enhancement is due to the reduction in polarization concentration and membrane fouling during nanofiltration process. K. Nagase et al. [13] have also found that the hollow fiber arrangement with parallel coiled hollow fibers is preferred than the straight parallel hollow fibers for enhancing oxygen transfer in an artificial gill using oxygen. This coiled hollow fibers module allows to uptake the oxygen from that dissolved in water. The enhancement of this rate is explained by the large mass transfer coefficient for the helical module. Liu et al. [14] have compared the performance of coiled hollow fiber membrane in membrane extraction to the straight hollow fiber. They found that improvement factor was in the range of 2–4. Zrelli et al. [15] have optimized the geometric configuration of a helically coiled fiber. This fiber is placed in the absorber, of the parabolic trough concentrator, in order to couple VMD with the solar energy. In this paper, we are trying to confirm the advantages of the use of helically coiled fiber for VMD coupled with solar energy. This confirmation is based on the comparison of the performance of coiled hollow fiber to those of linear fiber.

2. Material and methods

2.1. Setup

The design of solar thermal MD pilot plant (Fig. 1) is composed principally of parabolic trough concentrator. At the focal axis is mounted the absorber, which is in theshape of cylindrical tube. This absorber contains the hollow fibers membrane. The hollow fiber has, in the first case, the shape of coil. Hence, the configuration of absorber and membrane is similar to a helically coiled heat exchanger (Fig. 2(a)). In the second case, we use a linear hollow fiber. In order to compare the coil to the linear fibers, we conserve all fiber characteristics and we change only the geometric configuration. For the helically coiled fiber, we have used two fibers [15]. In order to conserve the same fiber exchange surface, we calculated the surface of the helical two fibers and we divided this obtained result by the surface of one linear fiber. The obtained value is the number of linear fibers which is 42. On the other hand and in the case of linear fiber, our study is interested in the domain shown in Fig. 2(b). Due to symmetry, the modeled domain is reduced to that presented in Fig. 3 (a). Also, for helically coiled fiber, the basic domain of study is presented in Fig. 3(b).

2.2. Mathematical model

Based on Figs. 2 and 3, we developed a mathematical model and the following assumptions are used for the numerical calculations:

(1) The flow is fully developed before it enters the inlet of the absorber.
(2) The fluid is incompressible and Newtonian.
(3) The gravity force is neglected.
(4) No slip condition is valid on the surface of fiber.

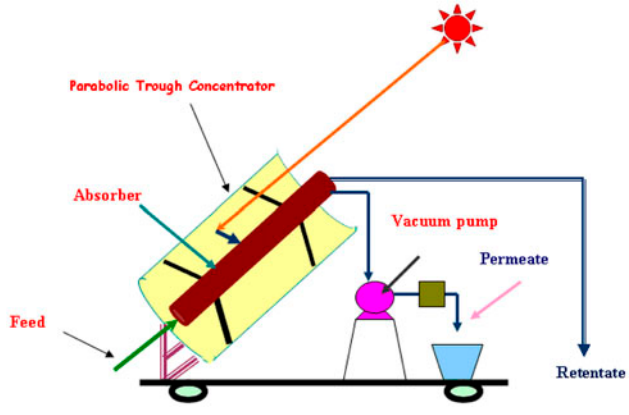

Fig. 1. Design of the thermal solar MD.

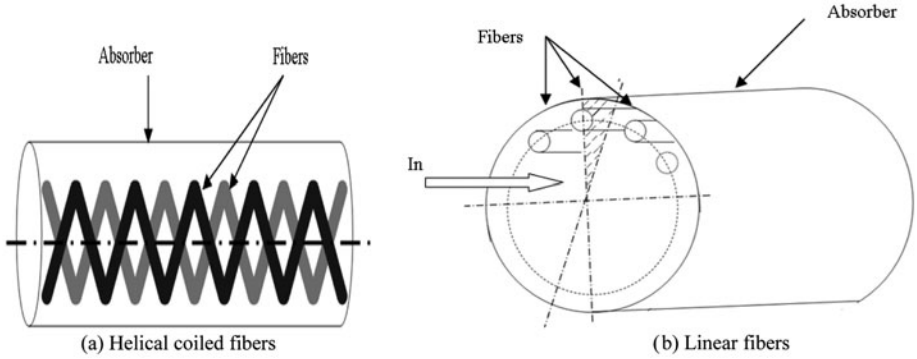

Fig. 2. Fibers in the solar concentrator absorber.

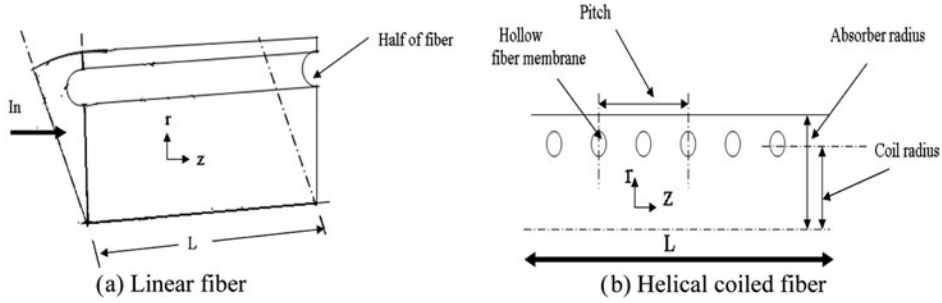

Fig. 3. Domain of the study.

(5) All simulations are carried out assuming steady state.
(6) The model is described in the coordinates r and z.

Under these conditions, the appropriate governing equations are written [16]:

Continuity equation:

$$\frac{\partial u_r}{\partial r}+\frac{u_r}{r}+\frac{\partial u_z}{\partial z}=0 \tag{1}$$

Momentum equations:

$$u_r\frac{\partial u_r}{\partial r}+u_z\frac{\partial u_z}{\partial z}=v\left[\frac{\partial}{\partial r}\left(\frac{1}{r}\frac{\partial r u_r}{\partial r}\right)+\frac{\partial^2 u_r}{\partial z^2}\right] \tag{2}$$

$$u_r\frac{\partial u_z}{\partial r}+u_z\frac{\partial u_z}{\partial z}=-\frac{1}{\rho}\frac{\partial P}{\partial z}+v\left[\frac{1}{r}\frac{\partial}{\partial r}\left(r\frac{\partial u_z}{\partial r}\right)+\frac{\partial^2 u_z}{\partial z^2}\right] \tag{3}$$

Energy equation:

$$u_r\frac{\partial T}{\partial r}+u_z\frac{\partial T}{\partial z}=\alpha\left[\frac{1}{r}\frac{\partial}{\partial r}\left(r\frac{\partial T}{\partial r}\right)+\frac{\partial^2 T}{\partial z^2}\right] \tag{4}$$

The boundary conditions for the velocity and the temperature are as follows:

At the inlet of the absorber, $Z=0$:

$$\begin{aligned} u_z &= 2u_0\left(1-\left(\tfrac{r}{R}\right)^2\right)\\ u_r &= 0\\ T &= T_{\text{in}} \end{aligned} \tag{5}$$

At the exit, $Z=L$:

$$u_r=\frac{\partial u_z}{\partial z}=\frac{\partial T}{\partial z}=0 \tag{6}$$

At the hollow fiber membrane surface:

$$\begin{aligned} u_z &= 0\\ u_r &= 0\\ T &= T_{\text{inter}} \end{aligned} \tag{7}$$

At the absorber interior wall, $r=R$:

$$\begin{aligned} u_z &= 0\\ u_r &= 0\\ T &= T_w \end{aligned} \tag{8}$$

The temperature at the feed/membrane interface (T_{inter}) is related to the bulk temperature (T_b) by the following heat balance equation [1,17]:

$$J_v L_v = h_f(T_b - T_{\text{inter}}) \tag{9}$$

The latent heat of vaporization of water (L_v) is given by [18]:

$$L_v = 2538.2 - 2.91T_{\text{inter}} \tag{10}$$

The absorber interior wall temperature (T_w) is given by the below equation:

$$T_w = T_e - \frac{q_u e}{\lambda_m} \tag{11}$$

where T_e is the absorber exterior wall temperature and q_u is the useful heat flow, given by:

$$q_u = q_a - q_e \tag{12}$$

$$k_m = 1.064\,\frac{r\varepsilon}{\delta\tau}\sqrt{\frac{1}{RT}} \tag{17}$$

The water vapor pressure (P_{inter}) at the liquid/vapor interface may be related with the temperature, by using the Antoine's equation [21]:

$$P_{\text{inter}}(T) = \exp\left(23.238 - \frac{3,841}{T-45}\right) \tag{18}$$

where $P_{\text{inter}}(T)$ is in Pa and T is in K.

In order to calculate the heat transfer coefficient, at the outside of the hollow fiber, we use the below equations [22–24]

Equation	Comments	Configuration	
$\text{Nu} = 19.64\text{Re}^{0.513}\ \text{Pr}^{0.129}\gamma^{0.938}$	60<Re<550, 0.058<γ<0.0955<Pr<7 $\gamma = \frac{P}{2\ piR_c}$	Helical	(19)
$\text{Nu} = 5.89\text{Re}^{0.443}\ \text{Pr}^{0.129}$	1<Re<500	Linear	(20)

The incident power of the absorber radiance, "q_a", is expressed by:

$$q_a = IC_g\rho\gamma\alpha\tau \tag{13}$$

The sum of the heat losses by convection and radiation between the absorber and the surrounding, "q_e", is given by [18]:

$$q_e = \varepsilon_a\sigma(T_e^4 - (T_a - 11)^4) + (5.7 + 3.8w_s)(T_e - T_a) \tag{14}$$

The thermal energy balance equation of the absorber "i" element (Fig. 4) is as follows:

$$q_u s_i = \dot{m}_{oi}\text{cp}T_{f_{oi}} - \dot{m}_{ii}\text{cp}T_{f_{ii}} + (\dot{m}_{ii} - \dot{m}_{oi})Lv \tag{15}$$

The dominant mechanism of mass transfer through the membrane pores at low vacuum pressures is Knudsen [11,19]. This model suggests a linear relationship between the permeate flux (J_v) and the transmembrane water vapor pressure difference (ΔP) [20]:

$$J_V = \frac{k_m}{\sqrt{M_w}}\,\Delta P = \frac{k_m}{\sqrt{M_w}}\,(P_{\text{inter}} - P_v) \tag{16}$$

The membrane permeability coefficient (k_m) can be related to membrane structural properties such as its membrane thickness (δ), pore tortuosity (τ), and pore radius (r) [1]:

The equations of temperature dependant properties, for water, are given by [25]:

$$\mu(T) = (-2.1897e-11)T^4 - (3.055e-8)T^3 + (1.6028e-5)T^2 - 0.0037524T + 0.33158 \tag{21}$$

$$\rho(T) = (-1.53629e-5)T^3 + 0.011778T^2 - 3.0726T + 1227.8 \tag{22}$$

$$k(T) = (1.5362e-8)T^3 - (2.261e-5)T^2 + 0.010879T - 1.0294 \tag{23}$$

$$\text{cp}(T) = (1.1105e-5)T^3 - 0.0031078T^2 - 1.478T + 4631.9 \tag{24}$$

For each 'i' element of the absorber, we can calculate the permeate flow rate '$\dot{m}_{pi}$' according to the below equation:

$$\dot{m}_{pi} = J_{vi}\pi L d_o \tag{25}$$

2.3. Solution procedure

The partial differential equations for continuity, momentum, and energy, Eqs. (1)–(4), are discretized

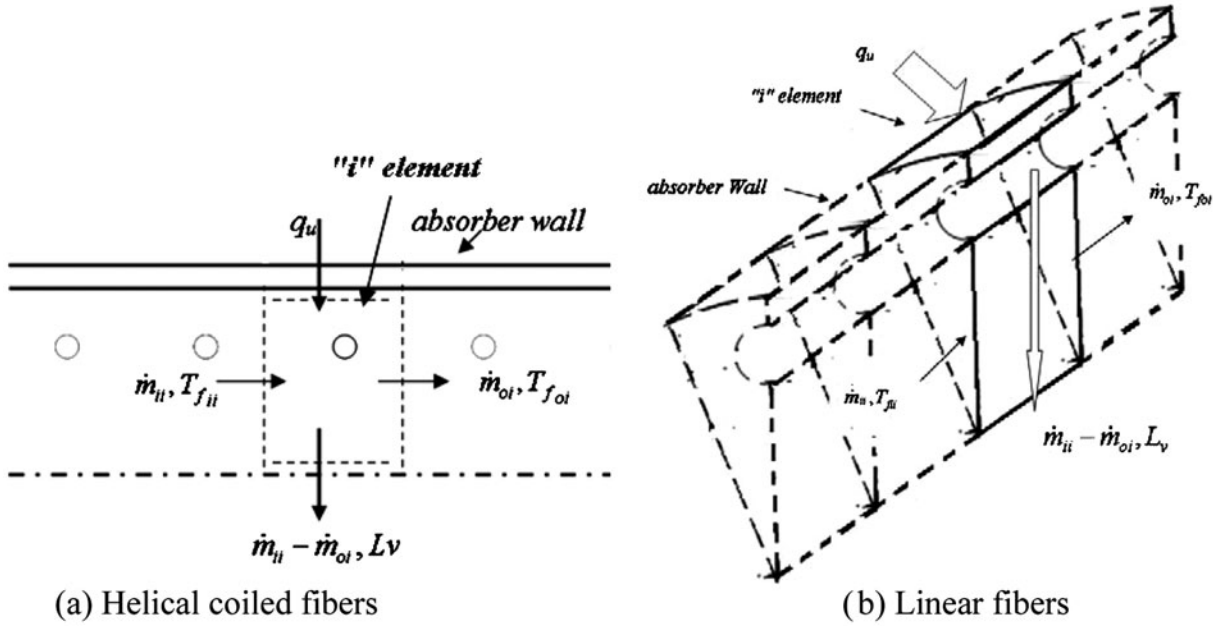

Fig. 4. Thermal balance on the "*i*" element of the absorber.

by means of a finite element method. The iteration procedure for the solution of coupled equations of hydrodynamics and heat transfer is as following:

(1) The velocity profile and the temperature in the inlet of the absorber are specified.
(2) For the calculation of the temperature distribution, all the membrane interfaces temperatures and the elementary external wall absorber temperatures were guessed.
(3) The absorber interior wall temperature (T_w) is determined by resolving the system of Eqs. (11)–(14).
(4) Solve energy equation, Eq. (4), at the boundary conditions, Eqs. (5)–(8), to obtain the bulk temperature for the first element of fiber.
(5) The membrane interface temperature for the first element fiber is determined by resolving the nonlinear system of Eqs. (9)–(10), (16)–(20).
(6) The resulting temperature was compared to the guessed value. In case the difference was greater than the tolerance limit (3×10^{-3}%), a new guess for the membrane interface temperature was applied, being the calculated value. When the difference between the two temperature values was within the prescribed limit, the corresponding temperature was taken as a boundary condition. So the permeate flux of the fiber element number "1" (J_{v1}) is determined also the permeate flow rate '$\dot{m}_{p1}$'. If the difference between '$\dot{m}_{p1}$' and the value of '$\dot{m}_{i1} - \dot{m}_{o1}$', given by Eq. 15, was greater than the tolerance limit (2%), a new guess for the elementary external wall temperature was applied. When the difference between the two values of the flow rates was within the prescribed limit, the permeate flow rate is determined. This procedure is then repeated for all elements of the absorber.

The flow chart for calculation is presented in Appendix.

All these steps were carried out on a PC with a CPU T 5200 1.6 GHz processor running under Windows XP pack3. The computed results were done using MATLAB and FemLab. The mesh characteristics present 7904 nodes.

3. Results and discussion

The results of our study, using two different configurations, helical, and linear, of hollow fibers having the same diameter and wall thicknesses will be presented now. The summery of the other properties are given in Tables 1 and 2. The liquid flow at the shell side is considered as Poiseuille flow. All simulations results are shown below.

Table 1
Design specifications and operating characteristics of fibers and membrane module

Property	Value
Length of the module (mm)	233
Module coil radius (mm)	195.2
Inner diameter of fiber (mm) [12]	0.27
outer diameter of fiber (mm) [12]	0.62
Pitch (mm)	25
Number of helical fibers	2
Inlet feed velocity (m/s)	3.4×10^{-4} (Re = 68)
Vacuum pressure (Pa)	1,000
Inlet feed temperature (°C)	20
Number of linear fibers	42
Number of helical fibers	2

Table 2
Geometrical and optical parameters of the absorber

Absorber configuration	Parameters
Length of the absorber (m)	0.233
Inside diameter of the absorber (mm)	206.5
Outside diameter of the absorber (mm)	219.1
Absorptivity of the absorber	0.9
Reflectivity of the absorber	0.9
Transmissivity	1
Intercept factor	0.9
Emissivity of absorber	0.9

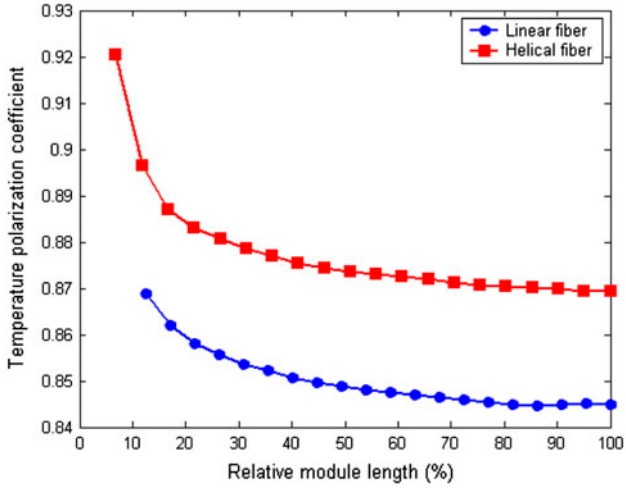

Fig. 5. Temperature polarization coefficient as function of relative module length for linear and helical fibers.

3.1. Effect of fiber configuration in temperature polarization coefficient

Fig. 5 illustrates the data obtained for the variations of the TPC (T_{inter}/T_b) for the two fiber configurations. These fibers are used in VMD coupled with solar energy in order to increase the temperature of the feed which flow in the shell side.

The inlet feed velocity, in this case, was 3.4×10^{-4} m/s corresponding to a Reynolds number of 68, and the inlet feed temperature was 20°C. According to this figure, two similar evolutions, of the TPC along the module length, were shown for the two fiber configurations. The value of the TPC drops quickly as module length increases from 0.1 to 0.3 for linear fiber and to 0.2 for helical fiber and then decreases slowly when module length increases to 1. For the linear fiber, the TPC decreases firstly from 0.8688 to 0.8543 and reaches the value of 0.8448 when the module length is 1. Also, for the helical fiber, the decrease, in the first, of the TPC was between 0.9205 and 0.8791 to reach, at the end, the value of 0.8695. However, the TPC of the helical fiber is greater than that of the linear fiber. The improvement factor of the TPC of the helical fiber is in the range of 3–6% compared to the linear one. This improvement can be explained by the fact that for the flow on the shell side of the helical fiber, a cross-flow is developed, of the hot feed in the outside surface of the helical fiber, which allows to enhance the outside heat transfer coefficient. Due to this enhancement, the interface outside membrane temperature (T_{inter}), for the helical fiber, is greater to that for linear fiber and in the same operating conditions.

3.2. Effect of fiber configuration in permeate flow rate

The improvement of T_{inter} leads to an increase in the permeate flow rate for the helical when it compared to the linear fiber (Fig. 6). According to this figure, the evolutions of the permeate flow rate along the module length increase from 2.7×10^{-2} to 3.58×10^{-2} kg/h for helical fiber and from 2.12×10^{-2} to 2.73×10^{-2} kg/h for linear fiber. In this case, the permeate flow rate for the helical fiber is 0.2685 and 0.21 kg/h for the linear fiber. The improvement factor in this case is about 28%. For the two configurations and along the module, the bulk temperature increases due to the solar rays focused on the exterior absorber wall. This increase in temperature raised the driving force, which is the vapor pressure difference (Eq. (16)) and the permeate flow rate. The difference between permeate flow rate for the helical and the linear fibers is principally due to the nature of the flow in the fiber

outside. In the case of the helical fiber, the cross-flow has an important influence on temperature polarization and permeate flow rate. However, cross-flow on the shell side yields a high heat transfer coefficient (Eq. (19)) than parallel flow in the case of linear fiber.

3.3. Effect of feed flow rate

The effect of feed flow rate was investigated at the range of 20–60 l/h (Re: 34–102). While the feed temperature was kept at 20 °C. The influence of feed flow rate on the permeate flow for linear and helical fibers is shown in Fig. 7. As shown, increasing the feed flow rate increased the permeate flow rate. The increase in feed velocity increases the Reynolds number, which causes the increase in the heat transfer coefficient in the outside boundary layer of the fiber. This improvement was not the same for both configurations. Fig. 8 illustrates the variation of the ratio between helical and linear permeate flow rate with the feed flow rate. It was found that this ratio increases strongly from 20 to 40 l/h then increases slowly from 1.28 to 1.31 when the feed flow increases from 40 to 60 l/h. It is important to remark that for the solar MD processes, the amount of energy collected is almost unchangeable for a specific day. For this reason and for our installation, the incident solar radiation is about 800 W/m^2, when the feed flow exceeds 40 l/h the residence time of the feed in the module decreases and the difference of the bulk temperature between the inlet temperature and the outlet temperature becomes smaller. So, optimization of the feed flow rate is an effective way to get high permeate flow rate in VMD coupled with solar.

3.4. Effect of inlet feed temperature

To obtain information about the effect of inlet feed temperature on the permeate flow rate, in both fiber configurations, feed temperature was varied in the range of 20–80 °C (Fig. 9) and the feed flow rate was fixed at 40 l/h. permeate flow rates for both configurations showed an exponential relationship with inlet feed temperature. Although For a given flow rate, feed temperature has small effect on the Reynolds number. There are only limited changes in viscosity and density. But the enhancement of the permeate flow rate with the inlet feed temperature can be explained by the increase in vapor pressure (Eq. (18)), or driving force ($P_{inter} - P_v$), with temperature. The helical fiber had higher permeated flow rate than that of linear fiber for all temperatures across the entire temperature range. Since the polarization coefficient temperature of the helical fiber was greater than in the linear fiber, T_{inter} in this case becomes close to the feed bulk temperature (T_b). This leads to had the evolution of the permeate flow rate between 0.746×10^{-4} kg/s and 5.139×10^{-4} kg/s when the inlet feed temperature increase from 20 to 80 °C.

4. Conclusions

In order to compare linear to helical fibers, in VMD coupled with solar energy, a mathematical model was developed. Also, the procedure for the solution of the resulting system of equations was presented. The

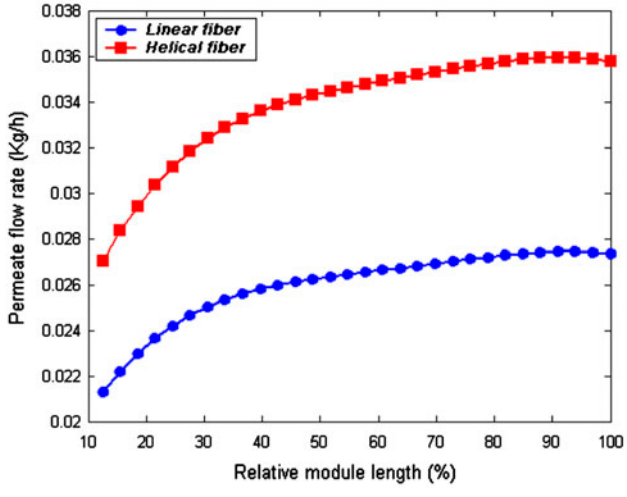

Fig. 6. Permeate flow rate vs. Relative module length for linear and helical fibers.

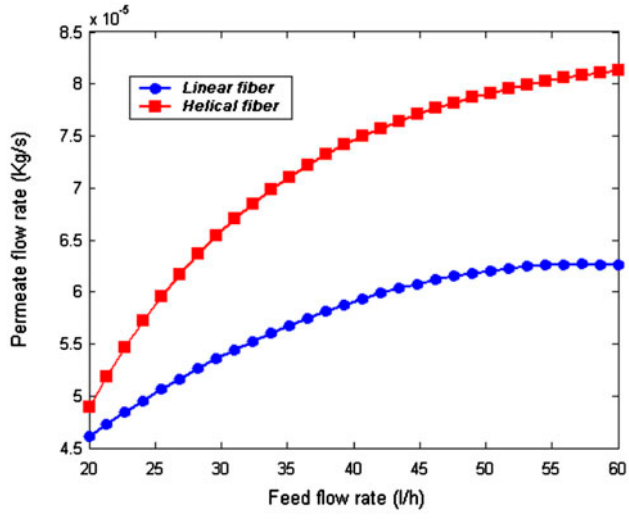

Fig. 7. Influence of feed flow rate on the permeate flow rate for helical & linear fibers.

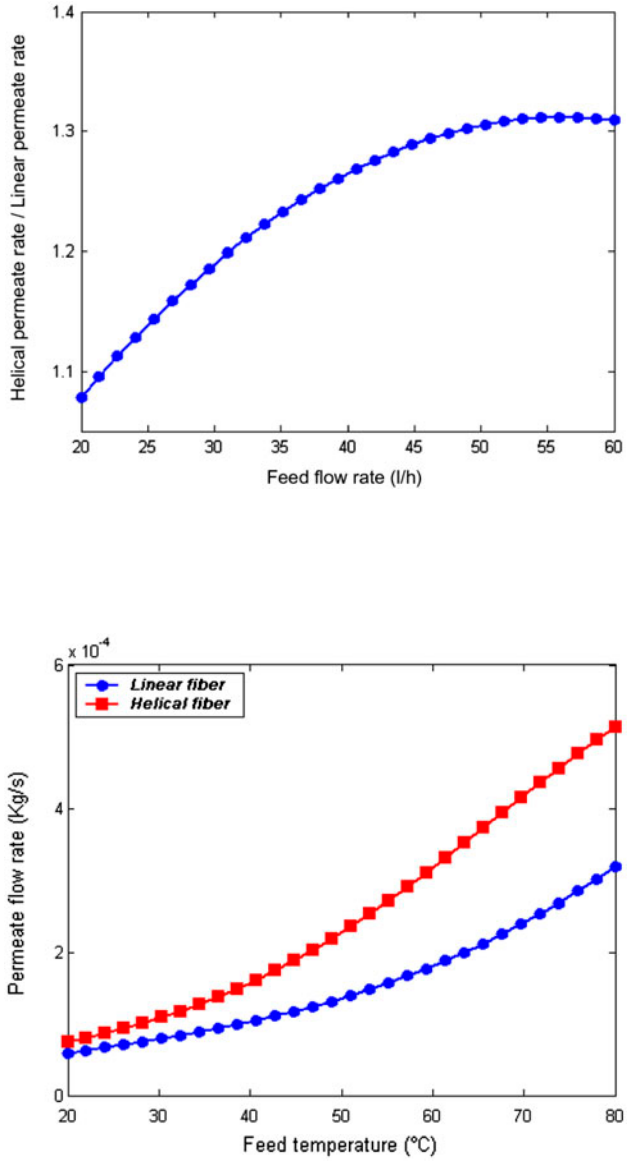

Fig. 9. Influence of feed temperature on the permeate flow rate.

results obtained prove that the TPC of the helical fiber are greater than that of the linear fiber. Hence, the improvement factor is in the range of 3–6%.

Due to this enhancement, the T_{inter} and consequently the permeate flow rate, for the helical fiber, were greater to that for linear fiber and in the same operating conditions. For the permeate flow rate, the improvement factor was 28%.

Aiming to investigate the effect of feed flow rate in the ratio between helical and linear permeate flow rate, feed flow was varied between 20–60 l/h. The results showed a clear improvement of the permeate flow rate about 31% in the case of the helical fiber. Also, the improvement of the permeate flow rate was in the range of 28–76% when the inlet of feed temperature was varied between 20 and 80 ℃.

Symbols

C_g — geometric concentration
cp — specific heat capacity, J/kg K
d — diameter, m
Dc — coil diameter, m
e — thickness of the wall absorber, m
h_f — boundary layer heat transfer coefficient of feed, W/m² K
I — incident radiation on the level of the concentrator, W/m²
J_v — permeate flux, kg/sm²
k — thermal conductivity, W/m k
k_m — membrane permeability coefficient, s mole$^{1/2}$ m^{-1} kg$^{-1/2}$
L — module length, m
Lc — length coil, m
L_v — latent heat of vaporization, J/kg
$\dot{m}_{ii}$ — feed flow rate in the inlet of element "i," kg/s
$\dot{m}_{pi}$ — permeate flow rate, kg/s
$\dot{m}_{oi}$ — feed flow rate in the outlet of element "i," kg/s
M_w — water molar mass, kg/mol
P — pressure, Pa/Pitch, m
P_{inter} — water partial pressure in the membrane surface, Pa
P_v — vacuum pressure, Pa
q_a — incident power of the absorber radiance, W/m²
q_e — heat flow loss, W/m²
q_u — useful heat flow, W/m²
r — radial coordinate
R — absorber radius, m
R_c — coil radius, m
s_i — outer side surface of the element "i" of the absorber, m²
T — temperature, K
u_0 — inlet average axial velocity, m/s
u_r — radial velocity, m/s
u_z — axial velocity, m/s
w_s — wind velocity, m/s
z — axial coordinate

Greek

α — Absorption coefficient of absorber/Thermal diffusivity, m²/s
ε_a — Emissivity of the absorber

γ — Interception coefficient of absorber/ dimensionless pitch
λ_m — Thermal conductivity of the absorber enlightened face, W/mK
μ — Dynamic viscosity, Kg/ms
v — Kinematic fluid viscosity, m^2/s
ρ — Reflectivity coefficient/Fluid density, Kg/m^3
σ — Stefan–Boltzmann constant, W/m^2K^4
τ — Transmission coefficient of absorber

Subscript

a — ambient
b — bulk
e — absorber external wall
f_{ii} — fluid at the entrance of the element "i" of the absorber
f_{oi} — fluid at the exit of the element "i" of the absorber
in — inlet
inter — interface membrane/feed
o — out
w — wall

References

[1] J.I. Mengual, M. Khayet, M.P. Godino, Heat and mass transfer in vacuum membrane distillation, Int. J. Heat Mass Transfer 47 (2004) 865–875.
[2] A.O. Imdakm, T. Matsuura, Simulation of heat and mass transfer in direct contact membrane distillation (MD): The effect of membrane physical properties, J. Membr. Sci. 262 (2005) 117–128.
[3] Y. Yun, R. Ma, W. Zhang, A.G. Fane, J. Li, Direct contact membrane distillation mechanism for high concentration Nacl solutions, Desalination 188 (2006) 251–262.
[4] C.M. Guijt, G.W. Meindersma, T. Reith, A.B. De Haan, Air gap membrane distillation. 2. Model validation and hollow fibre module performance analysis, Sep. Purif. Technol. 43 (2005) 245–255.
[5] R. Chouikh, S. Bouguecha, M. Dhahbi, Modelling of a modified air gap distillation membrane for the desalination of seawater, Desalination 181 (2005) 257–265.
[6] M. Khayet, M.P. Godino, J.I. Mengual, Theoretical and experimental studies on desalination using the sweeping gas membrane distillation method, Desalination 157 (2003) 297–305.
[7] F. Banat, S. Al-Asheh, M. Qtaishat, Treatment of waters colored with methylene blue dye by vacuum membrane distillation, Desalination 174 (2005) 87–96.
[8] S. Bandini, G.C. Sarti, Concentration of must through vacuum membrane distillation, Desalination 149 (2002) 253–259.
[9] S. Simone, A. Figoli, A. Criscuoli, M.C. Carnevale, A. Rosselli, E. Drioli, Preparation of hollow fiber membranes from PVDF/PVP blends and their applications in VMD, J. Membr. Sci. 364 (2010) 291–232.
[10] M. Safavi, M. Toraj, High-salinity water desalination using VMD, Chem. Eng. J. 149 (2009) 191–195.
[11] D. Wirth, C. Cabassud, Water desalination using membrane distillation: Comparison between inside/out and outside/ in permeation, Desalination 147 (2002) 139–145.
[12] H. Mallubhota, S. Hoffman, M. Schidt, J. Vente, G. Belfort, Flux enhancement during dean vortex tubular membrane nanofiltration. 10. Design, construction, and system characterization, J. Membr. Sci. 141 (1998) 183–195.
[13] K. Nagase, F. Kohori, K. Sakai, H. Nishide, Rearrangement of hollow fibers for enhancing oxygen transfer in an artificial gill using oxygen carrier solution, J. Membr. Sci. 254 (2005) 207–217.
[14] S.H. Liu, G.S. Luo, Y. Wang, Y.J. Wang, Preparation of coiled hollow-fiber membrane and mass transfer performance in membrane extraction, J. Membr. Sci. 215 (2003) 203–211.
[15] A. Zrelli, B. Chaouchi, S. Gabsi, Simulation of vacuum membrane distillation coupled with solar energy: Optimization of the geometric configuration of a helically coiled fiber, Desalin. Water Treat. 36 (2011) 41–49.
[16] R. Byron Bird, W.E. Stewart, E.N. Lightfoot, Transport Phenomena, second ed., John Wiley & Sons, Inc., New York, NY, 2002.
[17] J.P. Mericq, S. Laborie, C. Cabassud, Vacuum membrane distillation of seawater reverse osmosis brines, Water Res. 44 (2010) 5260–5273.
[18] B. Chaouchi, A. Zrelli, S. Gabsi, Desalination of brackish water by means of a parabolic solar concentrator, Desalination 217 (2007) 118–126.
[19] M.A. Izquierdo, G. Jonsson, Factors affecting flux and ethanol separation performance in vacuum membrane distillation (VMD), J. Membr. Sci. 214 (2003) 113–130.
[20] C. Cabassud, D. Wirth, Membrane distillation for water desalination: How to chose an appropriate membrane?, Desalination 157 (2003) 307–314.
[21] F. Banat, R. Jumah, M. Garaibeh, Exploitation of solar energy collected by solar stills for desalination by membrane distillation, Renewable Energy 25 (2002) 293–305.
[22] M.R. Salimpour, Heat transfer characteristics of a temperature-dependent-property fluid in shell and coiled tube heat exchangers, Int. Commun. Heat Mass Transfer 35 (2008) 1190–1195.
[23] M.R. Salimpour, Heat transfer coefficients of shell and coiled tube heat exchangers, Exp. Therm Fluid Sci. 33 (2009) 203–207.
[24] B. Li, K.K. Sirkar, Novel membrane and device for vacuum membrane distillation-based desalination process, J. Membr. Sci. 257 (2005) 60–75.
[25] J.S. Jayakumar, S.M. Mahajani, J.C. Mandal, P.K. Vijayan, Rohidas Bhoi Experimental and CFD estimation of heat transfer in helically coiled heat exchanger, Chem. Eng. Res. Des. 86 (2008) 221–232.

Appendix

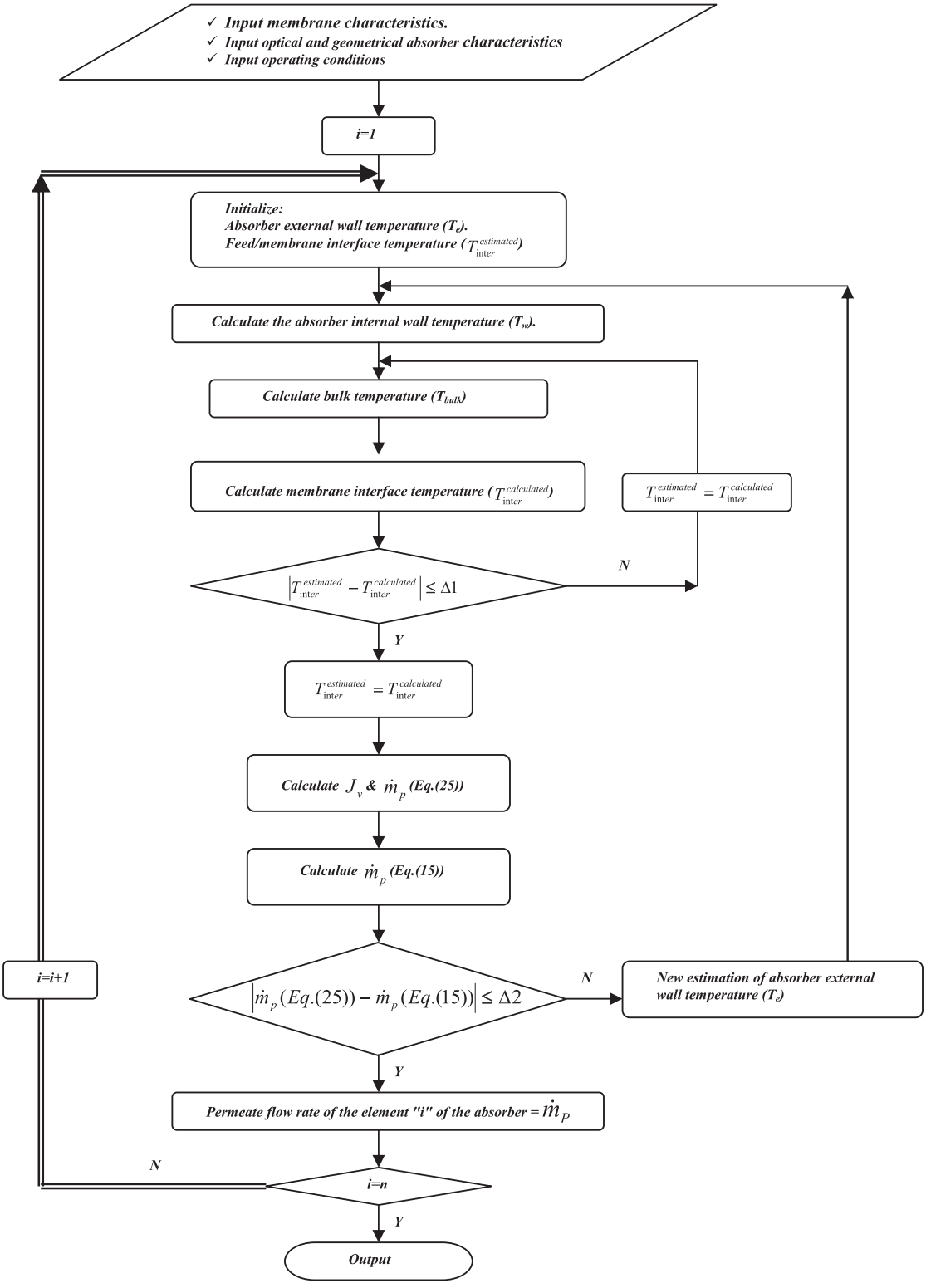

Flow chart for calculation